JACS
JOURNAL OF THE AMERICAN CHEMICAL SOCIETY
Article
Cite This: J. Am. Chem. Soc. XXXX, XXX, XXX−XXX
pubs.acs.org/JACS

Synthesis and Characterization of Non-Isolated-Pentagon-Rule Actinide Endohedral Metallofullerenes U@C_1(17418)-C_{76}, U@C_1(28324)-C_{80}, and Th@C_1(28324)-C_{80}: Low-Symmetry Cage Selection Directed by a Tetravalent Ion

Wenting Cai,[†,§,⊥] Laura Abella,[‡,⊥] Jiaxin Zhuang,[†,⊥] Xingxing Zhang,[†] Lai Feng,[∥] Yaofeng Wang,[†] Roser Morales-Martínez,[‡] Ronda Esper,[§] Mauro Boero,[#] Alejandro Metta-Magaña,[§] Antonio Rodríguez-Fortea,[‡] Josep M. Poblet,*[,‡] Luis Echegoyen,*[,§] and Ning Chen*[,†]

[†]Laboratory of Advanced Optoelectronic Materials, College of Chemistry, Chemical Engineering and Materials Science, Soochow University, Suzhou, Jiangsu 215123, PR China

[‡]Departament de Química Física i Inorgànica, Universitat Rovira i Virgili, c/Marcel·lí Domingo 1, 43007 Tarragona, Spain

[§]Department of Chemistry, University of Texas at El Paso, 500 W University Avenue, El Paso, Texas 79968, United States

[#]University of Strasbourg, CNRS, Institut de Physique et Chimie des Matériaux de Strasbourg UMR 7504, 23 rue du Loess, F-67034 Strasbourg, France

[∥]Soochow Institute for Energy and Materials InnovationS (SIEMIS), College of Physics, Optoelectronics and Energy & Collaborative, Soochow University, Suzhou, Jiangsu 215006, PR China

Supporting Information

ABSTRACT: For the first time, actinide endohedral metallofullerenes (EMFs) with non-isolated-pentagon-rule (non-IPR) carbon cages, U@C_{80}, Th@C_{80}, and U@C_{76}, have been successfully synthesized and fully characterized by mass spectrometry, single crystal X-ray diffractometry, UV−vis−NIR and Raman spectroscopy, and cyclic voltammetry. Crystallographic analysis revealed that the U@C_{80} and Th@C_{80} share the same non-IPR cage of C_1(28324)-C_{80}, and U@C_{76} was assigned to non-IPR U@C_1(17418)-C_{76}. All of these cages are chiral and have never been reported before. Further structural analyses show that enantiomers of C_1(17418)-C_{76} and C_1(28324)-C_{80} share a significant continuous portion of the cage and are topologically connected by only two C_2 insertions. DFT calculations show that the stabilization of these unique non-IPR fullerenes originates from a four-electron transfer, a significant degree of covalency, and the resulting strong host−guest interactions between the actinide ions and the fullerene cages. Moreover, because the actinide ion displays high mobility within the fullerene, both the symmetry of the carbon cage and the possibility of forming chiral fullerenes play important roles to determine the isomer abundances at temperatures of fullerene formation. This study provides what is probably one of the most complete examples in which carbon cage selection occurs through thermodynamic control at high temperatures, so the selected cages do not necessarily coincide with the most stable ones at room temperature. This work also demonstrated that the metal−cage interactions in actinide EMFs show remarkable differences from those previously known for lanthanide EMFs. These unique interactions not only could stabilize new carbon cage structures, but more importantly, they lead to a new family of metallofullerenes for which the cage selection pattern is different to that observed so far for nonactinide EMFs. For this new family, the simple ionic $A^{q+}@C_{2n}^{q-}$ model makes predictions less reliable, and in general, unambiguously discerning the isolated structures requires the combination of accurate computational and experimental data.

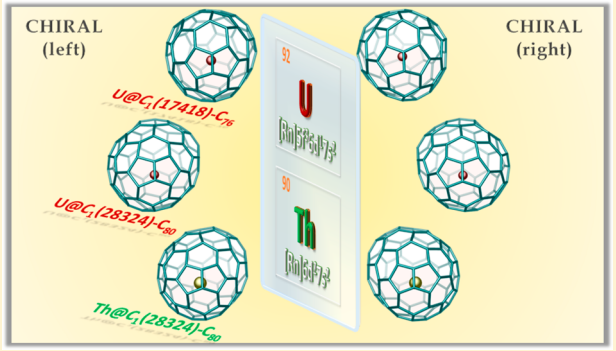

1. INTRODUCTION

Fullerenes are all-carbon molecules consisting of 12 pentagonal carbon rings and a variable number of hexagons.[1] So far, most experimental results showed that the pentagons on pristine empty fullerenes are surrounded by five hexagons, thus obeying the isolated pentagon rule (IPR).[2] However, the numbers of IPR cage isomers are very limited, whereas non-IPR fullerenes containing fused pentagons (pentalene units) are common and numerous. In contrast to IPR fullerenes, the non-IPR isomers

Received: September 27, 2018
Published: November 20, 2018

DOI: 10.1021/jacs.8b10435
J. Am. Chem. Soc. XXXX, XXX, XXX−XXX

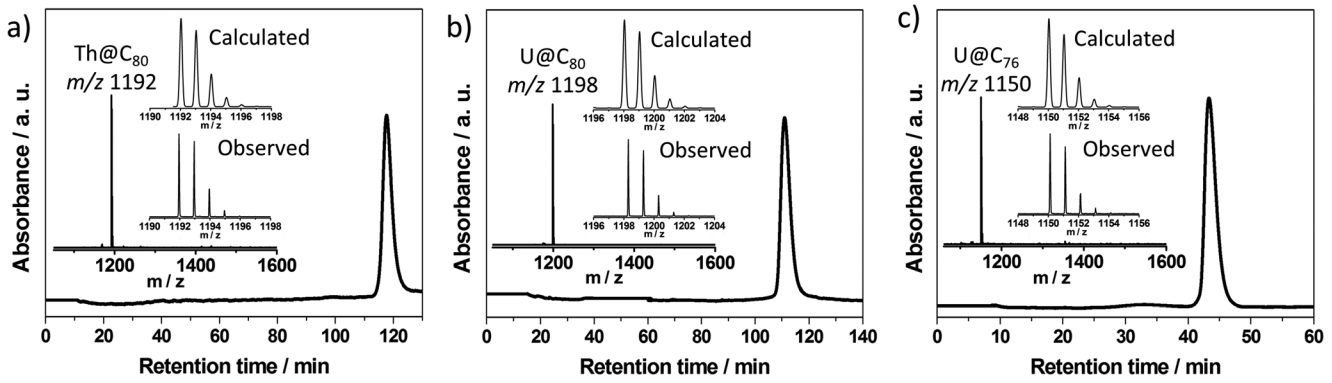

Figure 1. HPLC chromatograms of purified (a) Th@C_{80}, (b) U@C_{80}, and (c) U@C_{76} on a Buckyprep column with toluene as the eluent at flow rate of 4.0 mL·min^{-1}. Insets show the positive mode MALDI-TOF mass spectra and expansions of the experimental and theoretical isotopic distributions of Th@C_{80}, U@C_{80}, and U@C_{76}.

are strongly destabilized due to the enhanced local steric strain on the fused pentagons caused by enforced bond angles accompanied by higher pyramidalization of the carbon atoms.[3−5] Two strategies have shown practical effectiveness in generating non-IPR fullerene cages. One is exohedral halogenation so as to release the high bond strain of the fused pentagons.[6−11] For instance, some non-IPR fullerenes can be obtained as their chlorinated derivatives or perfluoroalkylated fullerenes.[9,12−14] However, the functionalized cages are severely distorted by the added groups, and some structures undergo skeletal transformations.

Endohedral metal doping is another practical way for the stabilization of non-IPR fullerenes without changing the cage framework. In these structures, substantial electron densities transferred from the encapsulated metallic species to the cages are significantly localized on the fused pentagons, and stabilization results from coordination of metal ions with the pentalene units.[1,15,16] To date, various non-IPR endohedral metallofullerenes (EMFs) with metallic clusters (i.e., M_2, M_3N, Sc_2S, Sc_2O; M = group 3 elements and most lanthanides) have been isolated and structurally characterized with X-ray crystallography such as $Sc_3N@D_3(6140)$-C_{68},[17] $Sc_2C_2@C_{2v}(6073)$-C_{68},[18] $Sc_3N@C_{2v}(7854)$-C_{70},[19] $Sc_2O@C_2(7892)$-C_{70},[20] $Sc_2S@D_2(10528)$-C_{72},[21] $M_2@D_2(10611)$-C_{72} (M = La, Ce),[22,23] $DySc_2N@C_s(17490)$-C_{76},[24] $M_3N@C_2(22010)$-C_{78} (M = Dy, Gd),[25,26] $M_3N@C_s(39663)$-C_{82} (M = Y, Gd),[27,28] and $Tb_3N@C_5(51365)$-C_{84}.[29] In contrast, most studies of non-IPR cages stabilized by single metallic species are limited to the realm of theoretical predictions, such as Ca@C_{72},[30] M@$C_1(17459)$-C_{76} (M = Yb, Ca, Sr, Ba),[31,32] M@$C_{2v}(19138)$-C_{76} (M = Sm, Yb, Ca, Sr, Ba),[31−33] and Th@$C_1(17418)$-C_{76},[34] whereas experimental studies are extremely rare. To the best of our knowledge, the only pristine mono-EMF possessing a non-IPR cage whose structure was unambiguously elucidated by single-crystal X-ray diffraction is Sm@$C_{2v}(19138)$-C_{76}.[33] In addition, a non-IPR La@C_{72} isomer was obtained in the form of La@$C_2(10612)$-$C_{72}(C_6H_3Cl_2)$, the result of synergistic stabilization from endohedral metal doping and exohedral derivatization.[35] This rare observation of non-IPR mono-EMFs seems to be ascribed to the relatively weak metal−cage interactions. Due to the very limited experimental results available, a deeper understanding of this phenomenon has never been fully addressed.

Recent success in the synthesis and characterization of a series of actinide EMFs demonstrated that actinide EMFs show substantially different electronic and chemical properties from those of the most extensively studied lanthanide EMFs.[34,36−41] In particular, different from the common Ln^{3+} charge state, actinides were found to adopt variable charge states depending on the cluster and the cage structures. For instance, four electrons of the Th atom are formally transferred to the $C_{3v}(8)$-C_{82} cage in Th@$C_{3v}(8)$-C_{82}.[38] The oxidation state of U in U@$D_{3h}(1)$-C_{74} and two U@C_{82} isomers, U@$C_2(5)$-C_{82} and U@$C_{2v}(9)$-C_{82}, can be 3+ or 4+, depending on the isomeric cage structure.[36] The very recent discovery of $U_2C@C_{80}$ even showed that U can take a formal 5+ charge state in the encapsulated cluster.[39] In contrast to the corelike 4f orbitals of the lanthanides, the 5f orbitals of the actinides are chemically accessible.[42,43] Thus, we anticipate that some previously undiscovered fullerene cage structures can be stabilized by encapsulating actinide metals, which may provide a new paradigm for metal−cage interactions and possibly alter some long-established principles based on the knowledge of lanthanide EMFs.

Herein, we report the synthesis, isolation and systematic characterization of three new non-IPR actinide EMFs, U@$C_1(17418)$-C_{76}, U@$C_1(28324)$-C_{80}, and Th@$C_1(28324)$-C_{80}. It is rather surprising to observe that two unanticipated non-IPR cage isomers $C_1(17418)$-C_{76} and $C_1(28324)$-C_{80}, which have never been observed before, were stabilized as actinide EMFs with a relatively high product yield. Combined experimental and computational studies have been performed to rationalize these unexpected results, which provide deeper understanding and new insights into the metal−cage interactions and stabilization of EMFs.

2. RESULTS AND DISCUSSION

2.1. Preparation, Purification, and Spectroscopic Characterizations of U and Th EMFs. Th@C_{80}, U@C_{80}, and U@C_{76} were synthesized by a modified direct current arc-discharge method.[44] The graphite rods packed with U_3O_8/graphite powder and ThO_2/graphite powder (molar ratio of M/C = 1:24) were annealed and then vaporized in the arcing chamber under a 200 Torr helium atmosphere. The collected raw soot was refluxed in CS_2 under an argon atmosphere for 12 h. Multistage HPLC separation procedures were employed to isolate and purify Th@C_{80}, U@C_{80} and U@C_{76} (see Figures S1−S3). The purity of the isolated Th@C_{80}, U@C_{80}, and U@C_{76} were confirmed by the observation of single peaks by HPLC (Figure 1a−c). The positive-ion mode MALDI-TOF mass spectra of the purified Th@C_{80}, U@C_{80}, and U@C_{76} show

DOI: 10.1021/jacs.8b10435
J. Am. Chem. Soc. XXXX, XXX, XXX−XXX

single peaks at 1192.077 , 1198.083, and 1150.120 m/z, respectively.

To obtain additional structural information for these new compounds, both vis−NIR and Raman spectroscopies were performed (see Figures S4 and S5). The vis−NIR absorption spectrum of U@C_{76} exhibits a distinct absorption at 593 nm, which differs from those reported for Sm@C_{2v}(19138)-C_{76}.[33] In addition, U@C_{80} exhibits only one broad absorption at 575 nm, while no obvious absorption was observed for Th@C_{80}. However, the low-energy Raman spectroscopic results show that the features of U@C_{80} around the cage vibration range are similar to those of Th@C_{80}, indicating that the cage isomer for U@C_{80} and Th@C_{80} is likely to be the same.

2.2. Crystallographic Identifications of U and Th based non-IPR EMFs. The three compounds under study were cocrystallized with Ni^{II}(OEP) (OEP = 2,3,7,8,12, 13,17,18-octaethylporphyrin dianion) to obtain good crystals suitable for X-ray measurements. Their molecular structures were determined with single crystal X-ray diffraction (XRD) crystallography. Notably, the fullerene cages for Th@C_{80}, U@C_{80}, and U@C_{76} are not the same isomers found for the previously reported $U_2C@I_h(7)$-C_{80},[39] $U_2@I_h(7)$-C_{80},[40] and Sm@C_{2v}(19138)-C_{76}.[33] In brief, both U@C_{80} and Th@C_{80} possess the same carbon cage with C_1 symmetry and one pair of fused pentagons, namely, the C_1(28324)-C_{80} cage. Similarly, U@C_{76} possesses the C_1(17418)-C_{76} cage with low symmetry and a fused pentagon pair as well. Interestingly, this cage was also predicted to be the most thermodynamically favorable candidate for a single Th atom at elevated temperatures.[34] Figure 2a−c show the molecular structures of these EMFs showing the major components together with the cocrystallized Ni^{II}(OEP) molecule. For all three compounds, the fused pentagons on the cages are close to the adjacent Ni^{II}(OEP) moieties. Interestingly, the porphyrin molecule faces a different side of the C_1(28324)-C_{80} cage when different metal atoms (U, Th) are encapsulated. The shortest distances between Ni and a cage carbon range from 2.954 to 3.024 Å, suggesting substantial $\pi-\pi$ interactions between the fullerene cages and Ni^{II}(OEP).

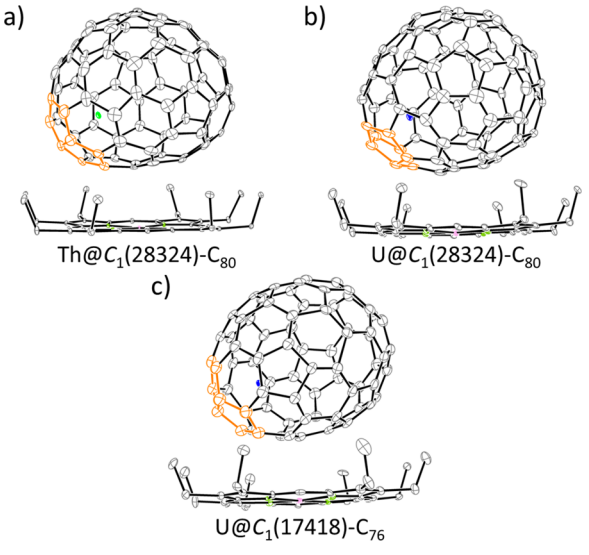

Figure 2. ORTEP drawings showing the relative orientations of the actinide endohedrals and porphyrin for (a) Th@C_1(28324)-C_{80}·Ni^{II}(OEP), (b) U@C_1(28324)-C_{80}·Ni^{II}(OEP), and (c) U@C_1(17418)-C_{76}·Ni^{II}(OEP). Thermal ellipsoids are shown at the 10% probability level and the fused pentagons in the cage framework are highlighted in orange. Only the major fullerene cage and the predominant uranium(or thorium) orientation are shown, and minor sites and solvent molecules are omitted for clarity.

2.2.1. Th@C_1(28324)-C_{80}. As shown in Figure 3a,b, a fully ordered non-IPR cage of C_1(28324)-C_{80} was clearly identified in the case of Th@C_1(28324)-C_{80}. Inside the fullerene cage, the thorium ion is slightly disordered over four positions (i.e., Th1, Th2, Th3, and Th4), which are short distances (0.9−3.4 Å) apart. The major Th site with 0.47 occupancy is residing very close to the edge of the fused pentagon pair with the distances ranging from 2.366 to 2.544 Å (see Figure S6 and Table S1), which are almost comparable to the shortest Th−C distances (i.e., 2.340(14)−2.494(10) Å) previously reported for Th@C_{3v}(8)-C_{82}.[38]

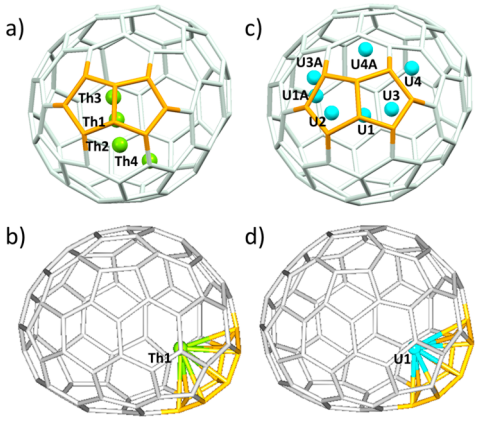

Figure 3. Perspective drawings show (a) the four positions of disordered thorium sites in Th@C_1(28324)-C_{80}; (b) the interaction of the major Th site Th1 with the closest cage portion; and (c) the positions of disordered uranium sites in U@C_1(28324)-C_{80}. The U atoms labeled with 'A' are generated by the crystallographic operation. (d) the interaction of the major U site U1 with the closest cage portion.

2.2.2. U@C_1(28324)-C_{80}. This crystal falls in the monoclinic $C2/m$ space group, as commonly encountered for many analogous EMF/Ni(OEP) systems, which contains two halves of the fullerene cage and a symmetry-related Ni(OEP) molecule.[45,46] Accordingly, an intact cage is obtainable by combining one-half of the cage with the mirror image of the other, both having an occupancy value of 0.50. Because the C_1(28324)-C_{80} cage is chiral, the two cage orientations are actually enantiomers. Figure S7 presents these two enantiomers (cages 1 and 1A), with the internal metal atom omitted for clarity. Inside the cage, the disorder of the U atom is different from that of the Th atom. There are four crystallographic sites for the uranium ion with occupancies of 0.32 for U1, 0.08 for U2, 0.08 for U3, and 0.02 for U4. Moreover, because only U2 resides at the symmetric plane, three additional metal sites (U1A, U3A, U4A) are generated via the crystallographic mirror plane (as shown in Figure 3c). Figure 3d shows the major site of the U atom (U1) in cage 1. Crystallographically, it is impossible to determine whether either or both of U1 and its mirror-related site U1A are occupied (see Figure S8). However, our calculations confirm that the U1 configuration is the most stable structure, while the U1A site does not lie at an energy minimum. Similar to the major Th site in Th@C_1(28324)-C_{80}, U1 is also located under the fused pentagons in the framework of C_1(28324)-C_{80}. However, the closest U−cage contacts for U1 were determined to be in the range of 2.267−2.640 Å, which are

DOI: 10.1021/jacs.8b10435
J. Am. Chem. Soc. XXXX, XXX, XXX−XXX

slightly shorter than the closest Th−cage contacts (see Figure S9 and Table S2).

2.2.3. U@C_1(17418)-C_{76}. This chiral fullerene cage is disordered with two enantiomers possessing nearly equal occupancy (cage 1/cage 2 = 0.58:0.42, as shown in Figure 4a). Within the cage, five U sites with fractional occupancies

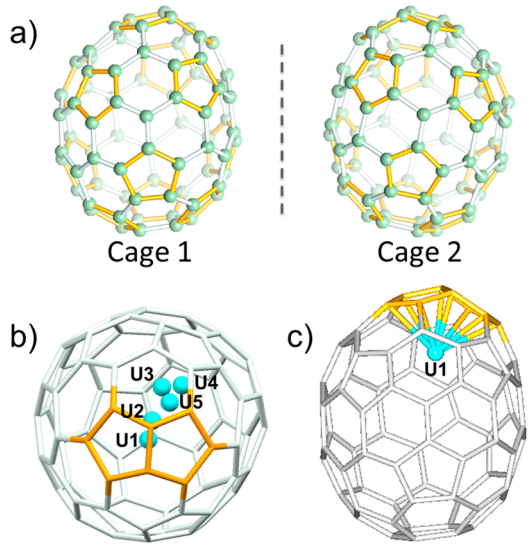

Figure 4. (a) Structures of two enantiomers of U@C_1(17418)-C_{76}. Internal disordered sites of uranium atom omitted for clarity. (b) Perspective drawing shows five positions of disordered uranium sites in the major enantiomer of C_1(17418)-C_{76} (cage 1). (c) View showing the position of U1 in cage 1.

ranging from 0.04 to 0.33 were identified. Figure 4b shows cage 1 with all the metal sites. A closer look reveals that both U1 and U2 sites are very close to the fused pentagons of this cage (as shown in Figure 4b). The shortest U−cage distances for U1 were determined to be in the range of 2.290−2.517 Å (see Figure S10 and Table S3).

It is worth noting that another C_{76} cage isomer, namely, C_1(17894)-C_{76}, was also considered at the very beginning. Topologically, the C_1(17894)-C_{76} cage can be obtained after only one Stone−Wales (SW) transformation step from the C_1(17418)-C_{76} cage (Figure 5). Crystallographic results

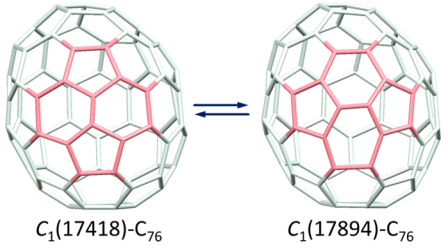

Figure 5. Structural similarity between C_1(17418)-C_{76} and C_1(17894)-C_{76}.

revealed that C_1(17894)-C_{76} exhibits very similar R_1 values to those of C_1(17418)-C_{76} (R_1(U@C_1(17894)-C_{76}) = 0.1283; R_1(U@C_1(17418)-C_{76}) = 0.1236). Consequently, it is difficult, if not impossible, to unambiguously assign which cage isomer we have based exclusively on the crystallographic analysis alone. Fortunately, in combination with the corresponding electrochemical and theoretical studies, the C_1(17418)-C_{76} cage was unambiguously assigned (see sections 2.4 and 2.5). This may be a rare case, but it raises a cautionary note for future structural analysis of fullerene cages, as it demonstrates that the SW related structures could be easily erroneously assigned by conventional crystallographic analyses alone. Thus, a combination of single-crystal X-ray characterization, theoretical calculations, and further structural characterizations is highly recommended to determine the final structural assignment.

2.2.4. Topological Connection between U@C_1(17418)-C_{76} and U@C_1(28324)-C_{80}. Interestingly, the U atom selects two non-IPR chiral carbon cages, C_1(17418)-C_{76} and C_1(28324)-C_{80}, that are intimately related. The two enantiomers of C_1(17418)-C_{76}, arbitrarily named **e1** and **e2**, share significant portions of their cage structures with the two enantiomers of C_1(28324)-C_{80} (Figure 6). In fact, enantiomer **e1** of C_1(28324)-

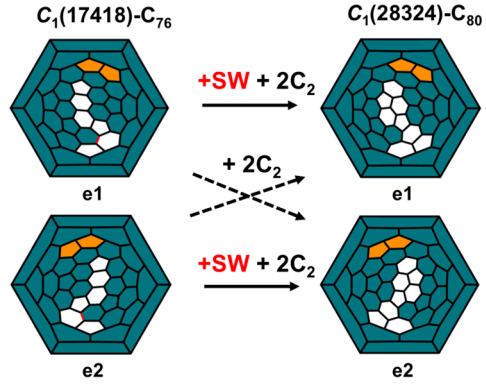

Figure 6. Schlegel diagrams showing topological links between chiral C_1(17418)-C_{76} and C_1(28324)-C_{80}. The dark blue regions correspond to the common parts shared by the two cages. The pentalene is highlighted in orange. The bond that rearranges through a SW transformation is highlighted in red. For a detailed description of the relationship between enantiomers **e1** (**e2**) of C_1(17418)-C_{76} and **e2** (**e1**) of C_1(28324)-C_{80}, see Figure S11.

C_{80} can be obtained after a Stone−Wales (SW) transformation on C_1(17418)-C_{76} (**e1**), followed by two consecutive C_2 insertions. A completely energetically equivalent chiral path exists that connects the other two enantiomers (**e2**). Remarkably, enantiomer **e1** (**e2**) of C_1(17894)-C_{76} and enantiomer **e2** (**e1**) of U@C_1(28324)-C_{80} are topologically connected by only two C_2 insertions with no further rearrangements; these paths would be less energetically demanding than those that preserve the same chirality (Figures 6 and S11 for more details). Therefore, these connections are enantiomerically dependent.

2.3. Electronic Structures and Isomer Abundances for Th@C_{80} and U@C_{80}. A detailed study was carried out to analyze the electronic structure of Th@C_{80} and U@C_{80} and to understand the key factors that govern the encapsulation of these two actinides. As observed in the X-ray structure, the optimal location of Th in Th@C_1(28324)-C_{80} is near the pentalene motif. This site maximizes the number of contacts between the metal ion and the neighboring carbon atoms, as shown in Figure 7b. The shortest computed values range between 2.50 and 2.69 Å, which are on average slightly longer than the experimental ones (Figure S6 and Table S2). Molecular orbital (MO) analysis confirmed the formal transfer of four electrons from the guest to the host upon encapsulation (Figure 8). Thus, the four valence electrons of the Th atom are transferred to the lower-lying unoccupied cage orbitals, which

DOI: 10.1021/jacs.8b10435
J. Am. Chem. Soc. XXXX, XXX, XXX−XXX

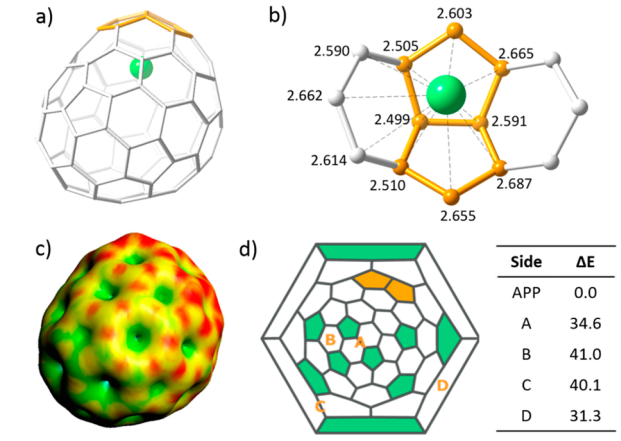

Side	ΔE
APP	0.0
A	34.6
B	41.0
C	40.1
D	31.3

Figure 7. DFT optimized structure (a); shortest Th−cage contacts (Å) (b); molecular electrostatic potential distribution for $C_1(28324)$-C_{80}^{4-} (c); and relative energies (in kcal·mol^{-1}) for several locations of Th inside $C_1(28324)$-C_{80} (d).

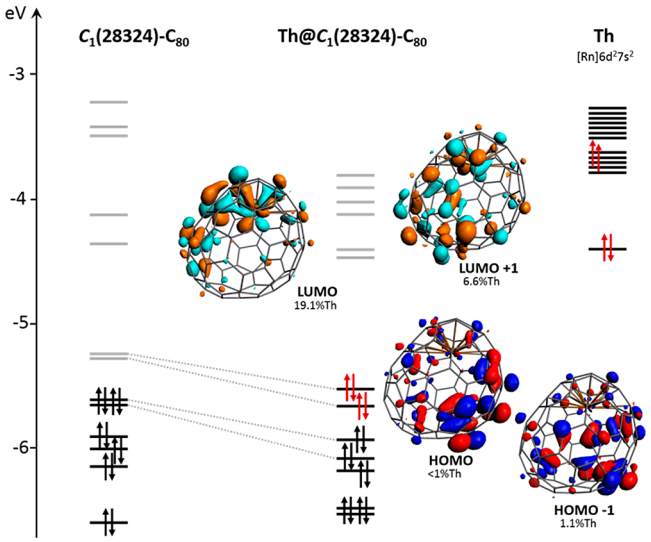

Figure 8. Orbital interaction diagram between Th and the C_{80} cage for Th@$C_1(28324)$-C_{80}. The contribution of Th orbitals to the MOs is also shown (in %). We represent the four highest energy electrons of Th@$C_1(28324)$-C_{80} in red, which are essentially in two cage orbitals, to denote the formal four-electron transfer from Th to the cage.

are mainly localized on the C_{80} framework. Several locations of Th within the fullerene were computed, and we found that the relative energies can vary significantly with the position of metal ion. It is evident from the values in Figure 7d that for an atom that behaves as a tetravalent cation the position closest to the pentalene is much more favorable than any other position. In particular, it is significantly lower in energy than those locations near the sumanene motifs (A and B in Figure 7d), which were recently found to show comparable energies to those near the pentalenes for a non-IPR C_{74} cage with one adjacent pentagon pair.[37]

For tetraanionic C_{80}^{4-} species, the highly symmetrical IPR I_h and D_{5h} are the carbon cages with the lowest energies. The most stable non-IPR tetraanions with one pentalene appear at relative energies between 30.9 and 36.1 kcal·mol^{-1} with respect to isomer I_h (Table 1). For anionic non-IPR cages, the pentalene motif concentrates a significant amount of the negative charge, as shown in the molecular electrostatic potential distribution and atomic charges computed for $C_1(28324)$-C_{80}^{4-} (Figurea 7c and S12). This electronic charge polarization is not a direct result of adding four electrons to molecular orbitals strongly localized on the pentalene. There is always a repolarization of the electronic density that results in a partial concentration of the negative charge on the pentalene due to its higher pyramidalization.[47] After the formal encapsulation of a tetravalent Th ion near the pentalene motif, all the non-IPR cages are significantly stabilized (Table 1). Compared to the other APP1 cages, this stabilization has a much more important impact on the observed $C_1(28324)$ cage, which can be attributed to the higher negative charge on the pentalene and to the larger number of Th−cage contacts (Table S1 and Figure S6). Thus, the observed $C_1(28324)$ non-IPR isomer and the IPR $C_{2v}(31922)$ and $D_{5h}(31923)$ cages were found within a range of energy less than 2 kcal·mol^{-1} (Table 1). Other GGA and hybrid density functionals were used to verify this result. Even though none of the tested functionals predicted the synthesized isomer Th@$C_1(28324)$ as the lowest in energy, we found it to be among those with the lowest energies (Tables S4−S6).

In a Krätschmer−Huffman reactor, the fullerenes are formed at very high temperatures (1500−3000 K).[44] Therefore, in addition to the potential energy differences, we have analyzed the relative stability of the most favorable EMFs in terms of their relative free energies, in order to incorporate thermal and entropic effects. The prediction of relative isomer concentrations requires determining the partition functions. The rotational−vibrational partition functions were constructed

Table 1. Relative Energies, Number of Adjacent Pentagon Pairs, Cage Symmetries, and Spin Densities for Selected Empty and Endohedral Metallofullerenes[a]

								U@C_{80} (Q)		U@C_{80} (T)		
isomer[b]	APP[c]	sym	C_{80} ΔE	C_{80}^{3-} ΔE	C_{80}^{4-} ΔE	La@C_{80} ΔE	Th@C_{80} ΔE	ΔE	SD[d]	ΔE	SD[d]	Sc_2O@C_{80} ΔE[e]
31920	0	C_{2v}	0.0	16.7	32.7	6.4	5.5			4.8	2.17	31.4
31922	0	C_{2v}	2.9	3.0	9.9	0.0	0.0	9.0	2.55	0.0	2.18	3.2
31923	0	D_{5h}	5.1	0.0	3.8	0.6	0.6	12.6	2.66	7.6	2.42	0.0
31924	0	I_h	16.2	4.2	0.0	13.0	11.6	17.1	2.50	17.3	2.21	4.0
28319	1	C_1	14.9	27.5	36.1	13.0	8.1	11.5	2.66	5.1	2.21	/
28324	1	C_1	21.5	28.0	31.4	13.7	1.4	13.5	2.66	0.5	2.21	16.9
31876	1	C_1	15.3	24.0	31.8	14.1	18.6	13.2	2.74	14.8	2.45	11.6
31891	1	C_1	19.1	25.7	30.9	21.0	23.2			20.7	2.35	27.4

[a]Energies are in kcal·mol^{-1}. [b]Isomer number according to the spiral algorithm by Fowler and Manolopoulos.[51] [c]Number of adjacent pentagon pairs (APP). [d]Mulliken spin density populations for U atoms in triplet and quintet states. [e]Values taken from ref 52.

DOI: 10.1021/jacs.8b10435
J. Am. Chem. Soc. XXXX, XXX, XXX−XXX

using the rigid rotor and harmonic oscillator (RRHO) approximation and the related free-encapsulated model (FEM) as proposed by Slanina.[48,49] The contribution due to chirality was also considered.[50] Both approximations predict the IPR Th@C_{2v}(31922)-C_{80} as the most abundant isomer up to around 1100 K. The experimentally observed structure, Th@C_1(28324)-C_{80}, was found to be the most abundant isomer above 1100 K within the FEM model (Figure 9), and the most

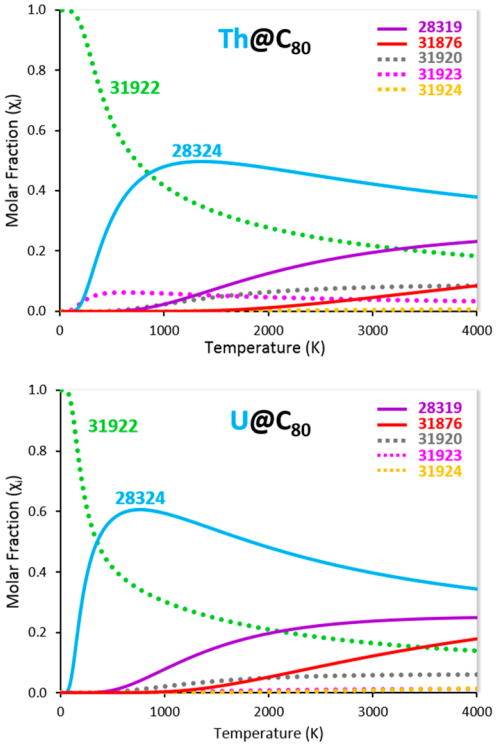

Figure 9. Computed molar fraction as a function of the temperature (K) using the free-encapsulating model (FEM) for the lowest-energy isomers of Th@C_{80} (top) and U@C_{80} (bottom). Dashed and continuous lines are used for IPR and non-IPR isomers, respectively.

abundant APP1 isomer in the whole range of temperatures in both approximations. The molar fractions of EMFs with highly symmetric cages (i.e., Th@D_{5h}(31923)-C_{80} and Th@I_h(31924)-C_{80}) are almost negligible in the whole range of temperatures.

Similar analysis was performed for the U@C_{80} family. Given that U retains two or three electrons in its valence shell, the ground state is not a singlet. We have optimized all eight isomers in Table 1 in triplet and quintet states. In the triplet state, the formal electron transfer between host and guest can be four or three electrons, while in the quintet state it must be three (see Scheme 1). Accordingly, the atomic spin densities (SD) computed for U range between 2.50 and 2.74 e for the quintet (f^3) and between 2.17 and 2.45 e for the triplet (f^2). We have not estimated the energies of triplet states with f^3 configuration for U, but we presume them to be similar to those for the quintet states, since the only difference among them is the magnetic interaction between a local magnetic moment of $S = 3/2$ in the U atom (f^3) and an unpaired electron on the cage, which can be coupled in either ferromagnetic (parallel) or antiferromagnetic (antiparallel) manner.

Like in the Th@C_{80} family, non-IPR U@C_1(28324)-C_{80} and IPR U@C_{2v}(31922)-C_{80} were found to be the lowest in energy,

Scheme 1. Schematic Representation of the Electronic Structure for $U^{3+}@C_{2n}{}^{3-}$ (Quintet or Triplet) and $U^{4+}@C_{2n}{}^{4-}$ (Triplet)

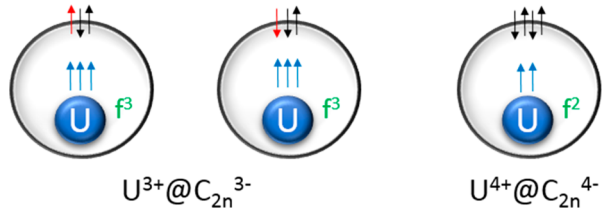

differing by only 0.5 kcal·mol^{-1}. Although at very low temperatures the IPR isomer is the dominant species, above 500 K the experimentally determined cage C_1(28324)-C_{80} is predicted to be the most abundant (Figure 9). In the two EMFs, the ground state corresponds to a triplet state, in which the metal is formally U^{4+}; the quintet states were computed between 9 and 13 kcal·mol^{-1} higher in energy than the corresponding triplet states. In fact, in six of the eight computed structures, the triplet state was easier to converge or lower in energy than the quintet. Only in one IPR and one non-IPR cage the triplet and quintet states were found to have similar energies. For U@C_{2v}(31920)-C_{80} and U@C_1(31891)-C_{80}, we were unable to converge a quintet state. These results suggest that U prefers to be in an oxidation state 4+ instead of 3+, even though for some carbon cages, it has been reported that the oxidation state 3+ is also an option for U.[36]

2.4. Computational analysis for U@C_{76}. After an initial screening of the lowest-energy tetraanions, we analyzed in detail the structure and relative energies of six isomers for U@C_{76}, the IPR isomer of T_d symmetry, and five non-IPR fullerenes with one adjacent pentagon pair (APP1). Among the tetraanions, the IPR cage is much lower in energy than the non-IPR ones (Table 2). However, as in C_{80}, the encapsulation of U alters significantly the relative stabilities of the five non-IPR isomers. Although the IPR EMF is still the lowest in energy, there are five isomers in a range of only 6 kcal·mol^{-1}. In Figure 10, we can observe that at very low temperatures the IPR isomer is the dominant species, but its concentration rapidly decreases when T increases. Contrarily, the abundance of the isolated and characterized U@C_1(17418)-C_{76} increases rapidly to a maximum at 500 K becoming the most abundant isomer up to 1000 K and the second most abundant isomer at higher temperatures. In contrast, the abundance of U@C_1(17894)-C_{76}, another possible isomer based exclusively on the crystallographic analysis, remains low below 1000 K but increases to a comparable level to that of the U@C_1(17418)-C_{76} at higher temperature. The ground state for U@C_1(17418)-C_{76} is a triplet with the two unpaired electrons localized on uranium. The theoretically predicted shortest U−C bond distances range between 2.41 and 2.52 Å, which agrees well with experimental results. A quintet state with formally three unpaired electrons on U and the fourth electron delocalized on the fullerene was found at +6.8 kcal·mol^{-1}. Electron spin density distributions (Figure S13) for the triplet and quintet states show the different nature of the two electronic states, which can be formally associated with oxidation states for U of 4+ and 3+, respectively. Despite this different nature, the uranium−carbon bond lengths are very similar for the two states, as shown in Table S7. To confirm these results, which show that there are several U@C_{76} isomers within a quite narrow energy range, we have explored other density functionals as well as introduced spin−orbit corrections (see last

DOI: 10.1021/jacs.8b10435
J. Am. Chem. Soc. XXXX, XXX, XXX−XXX

Table 2. Relative Energies and Atomic Spin Density Populations for Several EMFs with 76 Carbon Atoms[a]

				U@C_{76}(Q)		U@C_{76}(T)		
cage[b]	sym	C_{76}^{4-} ΔE	Th@C_{76} ΔE	ΔE	SD[d]	ΔE	SD[c]	U@C_{76}(SO) ΔE
19151	T_d	0.0	0.0	0.9	2.48	0.0	2.28	0.0
17418[d]	C_1	30.9	7.3	9.2	2.67	2.4	2.19	2.7
17459	C_1	24.5	14.6	4.5	2.60	4.8	2.21	5.3
17750	C_1	31.8	13.3	10.8	2.67	7.1	2.23	8.0
17894[e]	C_1	31.2	14.0	7.8	2.64	5.4	2.14	6.4
19138	C_{2v}	15.5	10.5	4.1	2.58	5.4	2.49	4.2
19142	C_s	29.5	31.2	23.6	2.73	23.0	2.44	

[a]Energies are in kcal·mol^{-1}. [b]All isomers are non-IPR (APP1) except the first one. [c]Mulliken atomic spin density population. [d]X-ray crystal structure for U@C_{76} and isomer proposed for Th@C_{76} by Zhao and co-workers.[34] [e]Non-IPR cage that also fits acceptably the X-ray diffraction data.

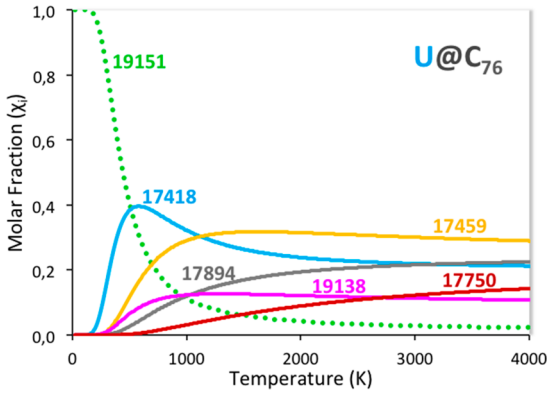

Figure 10. Computed molar fraction as a function of the temperature (K) using the free-encapsulating model (FEM) for the lowest-energy isomers of U@C_{76}.

column in Table 2) and similar results were obtained (Table S8).

2.5. Electrochemical Properties and Theoretical Analysis of Redox Potentials for U and Th Non-IPR EMFs. The electrochemical properties of Th@C_1(28324)-C_{80}, U@C_1(28324)-C_{80}, and U@C_1(17418)-C_{76} were investigated by means of cyclic voltammetry (CV) using a glassy carbon electrode with *ortho*-dichlorobenzene and tetra(*n*-butyl)-ammonium hexafluoro-phosphate (*o*-DCB/*n*-Bu_4NPF_6) as solvent/electrolyte (see Figure S14). Three reversible reductive steps and one reversible oxidative step were observed for U@C_1(17418)-C_{76}. However, for the other two compounds with the C_{80} cage, the electrochemical behavior is very different. Only the first redox process of U@C_1(28324)-C_{80} is electrochemically reversible, whereas all of the redox processes of Th@C_1(28324)-C_{80} are irreversible. The observed and computed redox potentials of U@C_1(17418)-C_{76}, U@C_1(28324)-C_{80}, and Th@C_1(28324)-C_{80} are summarized in Table 3 (see Table S9 for more details). The first reduction potential of Th@C_1(28324)-C_{80} is at −1.22 V, which is far more negative than that of U@C_1(28324)-C_{80}, resulting in a large electrochemical gap of 1.46 V, compared to 0.85 V for U@C_{80}. This large difference is somewhat unexpected since Th@C_{80} and U@C_{80} have the same cage structure and four electron charge transfer. Computed redox potential calculations in combination with MO analysis allow us to rationalize this significant difference. For Th@C_1(28324)-C_{80}, the Th 5f empty orbitals are quite high in energy, and the LUMO is localized on the carbon cage (Figure 8), but for U@C_1(28324)-C_{80} the energies of the U 5f orbitals are comparable to those of the cage orbitals (Figure S15).

Table 3. Comparison of Observed and Computed Redox Potentials[a]

species	isomer		$^{ox}E_1$	$^{red}E_1$	ΔE_{gap}
U@C_{76}	17418	exp.	0.14	−0.72	0.86
		DFT	0.12[b]	−0.85	0.97
	17894	DFT	−0.22[b]	−0.87	0.65
U@C_{80}	28324	exp.	0.28	−0.57	0.85
		DFT	0.26	−0.83	1.09
Th@C_{80}	28324	exp.	0.24	−1.22	1.46
		DFT	0.22	−1.28	1.51

[a]All values are given in V referred to Fc/Fc^+. [b]The computed values of the first oxidation potentials for Th@C_1(17418)-C_{76} and Th@C_1(17894)-C_{76} are +0.06 and −0.24 V, respectively.

Consequently, reduction processes are totally different, with reduction of the cage for Th@C_1(28324)-C_{80} at −1.22 V (computed −1.28 V) and reduction of the metal at a much lower potential of −0.57 V (computed −0.83 V) for U@ C_1(28324)-C_{80}. A simple inspection of the occupied frontier orbitals for these two EMFs leads to the conclusion that Th and U endohedral fullerenes should also display a quite different anodic peak, since for Th the oxidation should occur on the cage orbitals, whereas for U the oxidation should take place at the actinide. Nevertheless, to create an U^{5+} ion is very difficult, and all attempts to oxidize the U ion have failed, the result being that in both EMFs the oxidation occurs on the cage with similar oxidation potentials (0.22 V for Th vs 0.26 V for U). The overall consequence is that the EC gap for U@C_1(28324)-C_{80} is significantly smaller than for Th@C_{80}.

Concerning U@C_{76}, the comparison of observed and computed first oxidation and reduction potentials has been very useful in the final assignment of the carbon cage isomer (Table 3), as neither crystallographic analysis nor predicted abundances at high temperatures could completely discard one of the two possible non-IPR isomeric structures. In particular, the first oxidation potential strongly depends on the carbon cage. Hence, whereas the first oxidation potential for U@C_1(17418)-C_{76} is estimated from DFT calculations to be +0.12 V with respect to Fc/Fc^+, the corresponding value for isomer U@C_1(17894)-C_{76} is very negative, at −0.22 V. Since the oxidation occurs on the fullerene cage, quite similar values of +0.06 and −0.24 V were found for the corresponding Th analogues Th@C_1(17418)-C_{76} and Th@C_1(17894)-C_{76}. Clearly, the first oxidation potential for cage 17418 is much closer to the experimental value of +0.14 V. The difference observed for the two isomers can be easily rationalized from the HOMO energies of the corresponding U@C_{76} EMFs (see Figure 11). For

DOI: 10.1021/jacs.8b10435
J. Am. Chem. Soc. XXXX, XXX, XXX−XXX

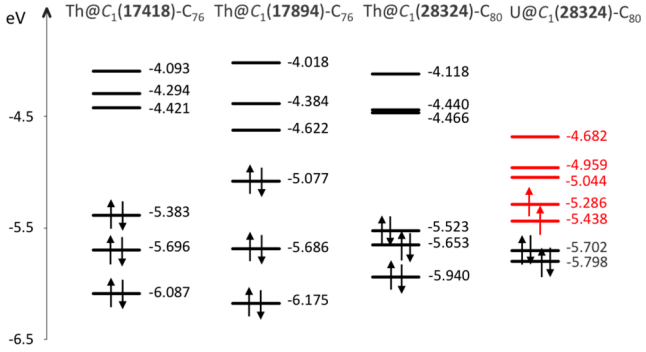

Figure 11. Schematic representation of selected frontier MOs for several Th and U EMFs. U(f) orbitals are presented in red.

simplicity, we have represented the MO energies for the Th derivatives since their ground states are always singlet states. The HOMO is about 300 mV lower in energy for U@C_1(17418)-C_{76}. In summary, combining all experimental and computational data, we conclude that the most likely isomer of the experimentally isolated U@C_{76} corresponds to U@C_1(17418)-C_{76}.

2.6. Why Are C_1(17418)-C_{76} and C_1(28324)-C_{80} Formed? Importance of Thermal Effects and Molecular Symmetry in Cage Selection. Soon after the discovery of Sc_3N@C_{80},[53] many theoretical studies highlighted the relevance of topology and the high symmetry of the icosahedral C_{80} cage when it encapsulates a guest that transfers six electrons to the carbon cage, as for example M_3N (M = Sc, Y, Lu, and other trivalent lanthanides with minor abundances),[54−57] La_2, or U_2.[40,58,59] For EMFs that show a 4-electron transfer, there is lower isomer selectivity and no prevalent cage exists in this case.

Since Th and U behave, in general, as tetravalent ions, in monoactinide EMFs there are important charge concentrations that induce strong interactions between the fullerene and the actinide. A direct consequence is that many non-IPR forms gain significant relative stability when the actinide is encapsulated. Nevertheless, this is not enough to completely reverse the relative energies of IPR and non-IPR EMFs, as shown in Tables 1 and 2. A key point is that the formation of fullerenes occurs at very high temperatures, and several other factors are also relevant at thermodynamic equilibrium. First, if the internal guest has mobility inside the fullerene, as assumed by the FEM model, then the symmetry of the fullerene cage is very relevant. For instance, fullerenes with I_h and D_{5h} symmetry contribute to the rotational partition function q_{rot} with values of the symmetry index σ equal to 60 and 10, respectively, whereas for a fullerene with C_1 symmetry the corresponding value is 1. Car−Parrinello molecular dynamics simulations carried out for U@C_{80} have shown that U has rather limited mobility at 300 K, but much higher mobility at temperatures of fullerene formation (Figure 12). This fact justifies the use of the FEM model in our isomer abundance analysis.

A second factor to be accounted for in cage selection at high temperatures is that nonsymmetric cages are chiral. Given that the overall partition function q is inversely proportional to the symmetry index σ and directly proportional to the chirality contribution (1 for nonchiral systems and 2 for chiral),[50] carbon cages with C_1 symmetry have increased abundances when T is increased. Therefore, for C_{2n} fullerenes with a high number of IPR isomers with C_1 symmetry the probability of capturing non-IPR cages would be very small. However, we recently reported

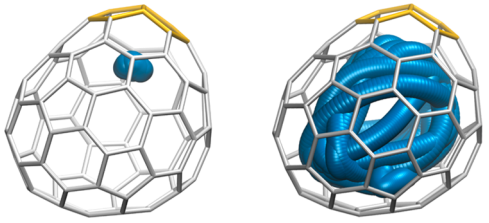

Figure 12. Car−Parrinello molecular dynamics trajectories at 300 K (left) and 1500 K (right) for U@C_1(28324)-C_{80}. The motion of the internal U atom is shown in blue. The pentalene is highlighted in orange.

the IPR U^{4+}@D_{3h}-C_{74}.[36,53] With 74 atoms, there is only one IPR isomer and three isomers containing a pentalene (APP1). The IPR cage is between 15 and 34 kcal·mol^{-1} lower in energy than the APP1 isomers (Table S10). The capture of isomer D_{3h} occurs because it does not lose too much stability with respect to the non-IPR EMFs once U is encapsulated. This happens because it has a particular structure that results in a short uranium-fullerene bond distance, 2.35 Å (DFT), the shortest among all the uranofullerenes analyzed so far. Consequently, the thermal and entropic effects cannot counterbalance the energy differences; hence, the IPR form is the dominant one up to 2800 K (Figure S16). Similar results were found for Th@C_{74}.[37] Therefore, highly symmetric EMFs are only formed during the arc-discharging process preferentially when their relative energies with respect to the less symmetric EMFs are large enough. The prototypical example is I_h-C_{80}, which is able to encapsulate many different guests that can exhibit a six-electron transfer. Among them, Sc_3N@C_{80} is the most relevant, since it is the third most abundant fullerene after C_{60} and C_{70}. In other words, temperature works against symmetry, but it does not always win.

2.7. Covalency of Actinide−Fullerene Interactions. The existence of formal Th^{4+} or U^{4+} ions interacting with C_{2n}^{4-} cages and the fact that the computed encapsulation energies correlate with the amount of charge transferred (Tables S11 and S12) lead us to assume that the metal−cage interaction can be described as essentially ionic, as found for other families of cluster fullerenes. It is remarkable that covalent contributions to metal−cage interactions were found to be non-negligible.[60,61] Recently, the Th−cage interaction was analyzed for several Th@C_{2n} systems, and in addition to the strong metal−cage electrostatic attraction, significant covalent Th−cage interactions were found, which were larger than those for lanthanide EMFs.[34,37] From a comparison between Th@C_{80} and U@C_{80}, we have found some evidence that the U−cage interactions show a higher degree of covalency than for Th−cage ones, in line with the smaller electronegativity difference, 0.85 vs 1.25 units in the Pauling scale for U−C and Th−C, respectively. Appreciably higher mixing and overlapping of the 5f orbitals of the actinide with the cage was observed for U@C_{80} compared to Th@C_{80} (see Figures 7 and S15). Additionally, focusing on the topology of the molecular electron density (QTAIM),[62] we found that the descriptors at the actinide−cage bond critical points (BCP), as for example the density, kinetic or potential (or total) energy densities, and Mayer bond order (MBO), indicate somewhat larger covalency (largest values) for the U−C interaction, in line with the shorter U−C distances; see Table 4. In agreement with the higher ionicity for Th endohedral fullerenes, the computed Bader atomic charge is more positive when the encapsulated metal is Th (+2.12 e) than when it is U (+1.70 e). Therefore, this

DOI: 10.1021/jacs.8b10435
J. Am. Chem. Soc. XXXX, XXX, XXX−XXX

Table 4. Metal Atomic Charges and Selected M−Cage Bonding Descriptors for M@C_1(28324)-C_{80}[a,b]

M	q(M)[c]	d(M−C)	MBO	ρ_{bcp}	$H(r)/\rho_{bcp}$
U	+1.70	2.42	0.356	0.523	−0.279
Th	+2.12	2.50	0.307	0.475	−0.260

[a]Average values for the three shortest M−C contacts. [b]Distances in Å; charges in e; MBO is the Mayer bond order; ρ_{bcp} is the electron density at bond critical point (in e Å^{-3}); $H(r)/\rho_{bcp}$ is the normalized total energy density (in h e^{-1}). [c]Bader atomic charges determined from ADF code.

preliminary analysis leads us to conclude that the degree of covalency in the U−cage interactions should be higher than for the Th−cage interactions, but more extensive studies for other cages, which are now under way, are required to further generalize this statement.

3. CONCLUSIONS

For the first time, actinide EMFs with non-IPR cages, U@C_{80}, Th@C_{80}, and U@C_{76}, have been successfully synthesized and characterized by mass spectrometry, single crystal X-ray crystallography, UV−vis−NIR and Raman spectroscopy, cyclic voltammetry, and DFT calculations. Crystallographic analyses revealed that the U@C_{80} and Th@C_{80} share the same non-IPR cage, C_1(28324)-C_{80}. Combined experimental and theoretical studies were performed to assign U@C_{76} to U@C_1(17418)-C_{76}, which is intimately related to C_1(28324)-C_{80}.

Results from DFT calculations show that the encapsulation of Th and U ions shows similarities, but the actinide EMFs present significant electronic and physicochemical differences. The stabilization of some non-IPR fullerenes originates from strong host−guest interactions. This is particularly true in the encapsulation of tetravalent cations, where the interactions between the cation and the pentalene motif for the non-IPR fullerene are much stronger than for fullerenes that host clusters with trivalent metals, such as, Sc_2O, Sc_2C_2, and so on.

The actinide ion displays high mobility within the fullerene; therefore, both the symmetry and the chirality of the carbon cage play important roles to determine the isomer abundances at temperatures at which fullerenes are formed. Chiral cages with low symmetry are thermodynamically favored at high temperatures with respect to nonchiral high-symmetry ones. This is the reason why chiral non-IPR isomers of C_1 symmetry can be competitive in some circumstances, like in the formation of U@C_{76}, U@C_{80}, and Th@C_{80}.

Molecular orbital analysis and electron density bond descriptors show that the degree of covalency for the actinide−cage interactions is higher for U than for Th, in line with the greater electronegativity of U with respect to Th.

Finally, it is worth noting that the structural assignment of U@C_1(17418)-C_{76} via crystallographic analysis alone resulted in two equally probable cages that satisfied the experimental diffraction data. In situations like this, which are likely to be observed in future work with endohedral fullerenes, where many isomeric cage structures can be observed, the use of other characterization techniques as well as accurate DFT calculations seems essential.

4. EXPERIMENTAL SECTION

4.1. Synthesis and Isolation of Th@C_{80}, U@C_{80}, and U@C_{76}. The carbon soots containing actinide EMFs were synthesized by the direct-current arc discharge method. The graphite rods, packed with ThO_2/graphite powder and U_3O_8/graphite powder (molar ratio of M/C = 1:24), were vaporized in the arcing chamber under 200 Torr He atmosphere. The resulting soot was refluxed in CS_2 under an argon atmosphere for 12 h. The separation and purification of Th@C_{80}, U@C_{80}, and U@C_{76} were achieved by multistage HPLC procedures. Multiple HPLC columns, including Buckyprep-M column (25 × 250 mm, Cosmosil, Nacalai Tesque Inc.), Buckprep-D column (10 × 250 mm, Cosmosil, Nacalai Tesque, Japan), and Buckprep column (10 × 250 mm, Cosmosil, Nacalai Tesque, Japan), were utilized in this procedure. Further details are described in the Supporting Information.

4.2. Spectroscopic Studies. The positive-ion mode matrix-assisted laser desorption/ionization time-of-flight (MALDI) was used for mass characterizations. UV−vis−NIR spectra of the purified Th@C_{80}, U@C_{80}, and U@C_{76} in CS_2 solution were measured with a Cary 5000 UV−vis−NIR spectrophotometer (Agilent, USA). Raman spectra were recorded on a Horiba Lab RAM HR Evolution Raman spectrometer using a laser at 633 nm.

4.3. Electrochemical Studies. CV results were obtained in *o*-dichlorobenzene using a CHI-660E instrument. A conventional three-electrode cell consisting of a platinum counterelectrode, a glassy carbon working electrode, and a silver reference electrode was used for all measurements. (n-Bu)$_4$NPF$_6$ (0.05 M) was used as the supporting electrolyte. The CVs were measured at a scan rate of 100 mV/s.

4.4. Single-crystal X-ray diffraction. Crystalline blocks of U@C_{2n} ($2n$ = 76, 80) and Th@C_{80} were obtained by layering a benzene or chloroform solution of Ni^{II}(OEP) over a nearly saturated solution of the respective endohedral in CS_2 in a glass tube. Over a 20 day period, the two solutions diffused into each other, and black crystals formed. XRD measurements were performed at 150 K on a Bruker P4 machine equipped with a graphite monochromator. The multiscan method was used for absorption corrections. The structures were solved by a direct method and were refined with SHELXL-2013.[63] Hydrogen atoms were inserted at calculated positions and constrained with isotropic thermal parameters.

4.4.1. Crystal Data for U@C_1(17418)-C_{76}·Ni^{II}(OEP)·($CHCl_3$). $C_{113}H_{45}Cl_3N_4NiU$, M_w = 1861.62, monoclinic, space group $P2/c$, a = 18.686(5) Å, b = 15.184(4) Å, c = 25.496(6) Å, β= 91.390(6)°, V = 7232(3) Å^3, Z = 4, T = 150 K, ρ_{calcd} = 1.710 Mg m^{-3}, μ(Mo Kα) = 2.672 mm^{-1}, 19 995 reflections measured, 11 652 unique (R_{int} = 0.0879 used in all calculations. The final wR_2 was 0.3750 (all data) and R_1 (6682 with $I > 2\backslash s(I)$) = 0.1236. CCDC 1835947 contains the crystallographic data.

4.4.2. Crystal Data for U@C_1(28324)-C_{80}·Ni^{II}(OEP)·2($CHCl_3$). $C_{118}H_{46}Cl_6N_4NiU$, M_w = 2029.03, monoclinic, space group $C2/m$, a = 25.180(3) Å, b = 15.2158(18) Å, c = 19.325(2) Å, β = 92.509(2)°, V = 7397.1(15) Å^3, Z = 4, T = 100 K, ρ_{calcd} = 1.822 Mg m^{-3}, μ(Mo Kα) = 2.725 mm^{-1}, 37 119 reflections measured, 7864 unique (R_{int} = 0.1010 used in all calculations. The final wR_2 was 0.3941 (all data) and R_1 (4835 with $I > 2\backslash s(I)$) = 0.1285. CCDC 1862103 contains the crystallographic data.

4.4.3. Crystal Data for Th@C_1(28324)-C_{80}·Ni^{II}(OEP)·2(C_6H_6). $C_{128}H_{56}N_4NiTh$, M_w = 1940.51, monoclinic, space group $C2/c$, a = 45.4289(8) Å, b = 15.0655(3) Å, c = 25.2663(4) Å, β= 120.3020(10)°, V = 14929.9(5) Å^3, Z = 8, T = 173 K, ρ_{calcd} = 1.727 Mg m^{-3}, μ(Mo Kα) = 7.234 mm^{-1}, 86 356 reflections measured, 13 701 unique (R_{int} = 0.0377 used in all calculations. The final wR_2 was 0.2743 (all data) and R_1 (12504 with $I > 2s(I)$) = 0.0967. CCDC 1862104 contains the crystallographic data.

4.5. Computational Details. The geometry optimizations were performed at the DFT level with the ADF 2013 program.[64,65] The PBE functional and Slater TZP basis sets (PBE/TZP level) were used for most of the calculations. Relativistic corrections were included by means of the ZORA formalism. Oxidation and reduction potentials were calculated at the BP86/TZP level with the inclusion of solvent effects by means of the COSMO model.

Molecular dynamics simulations were carried out using Car−Parrinello Molecular Dynamics (CPMD) program.[66,67] The description of the electronic structure was based on the expansion of the valence electronic wave functions into a plane wave basis set, which was limited by an energy cutoff of 100 Ry. The interaction between the

DOI: 10.1021/jacs.8b10435
J. Am. Chem. Soc. XXXX, XXX, XXX−XXX

valence electrons and the ionic cores was treated through the pseudopotential (PP) approximation (Martins−Troullier type for C and Goedecker−Teter−Hutter type for U). The PBE functional was selected. The simulations were carried out in a cubic cell with a side length of 14 Å, a fictitious electron mass of 3100 a.u., and a time step of 0.121 fs.

Bond critical point (BCP) descriptors for Th@C_1(28324)-C_{80} and U@C_1(28324)-C_{80} were obtained using the Multiwfn program.[68] Wave functions used for the analysis were obtained from Gaussian 16.[69] Geometry optimizations were performed at the DFT level using the PBE functional. A double-ζ 6-31G(d,p) basis set was used for C atoms and Stuttgart−Dresden basis sets with effective core potential (SDD) for Th and U atoms.[70]

A data set collection of computational results is available in the ioChem-BD repository[71] and can be accessed via https://doi.org/10.19061/iochem-bd-2-31.

■ ASSOCIATED CONTENT

Supporting Information

The Supporting Information is available free of charge on the ACS Publications website at DOI: 10.1021/jacs.8b10435.

HPLC profiles for the separation of Th@C_1(28324)-C_{80}, U@C_1(28324)-C_{80}, and U@C_1(17418)-C_{76}. UV−vis−NIR absorption spectra and low energy Raman spectra of Th@C_1(28324)-C_{80}, U@C_1(28324)-C_{80}, and U@C_1(17418)-C_{76}. Cyclic voltammetry of Th@C_1(28324)-C_{80}, U@C_1(28324)-C_{80}, and U@C_1(17418)-C_{76} in *o*-dichlorobenzene containing 0.05 M *n*-Bu_4NPF_6. Additional results from computations on Th@C_1(28324)-C_{80}, U@C_1(28324)-C_{80}, and U@C_1(17418)-C_{76} and related systems (relative energies with different functionals, M−C distances, spin densities, MO diagrams, etc.) (PDF)

Crystallographic information files for U@C_1(17418)-C_{76}·Ni^{II}(OEP)·($CHCl_3$), Th@C_1(28324)-C_{80}·Ni^{II}(OEP)·2(C_6H_6), and U@C_1(28324)-C_{80}·Ni^{II}(OEP)·2($CHCl_3$) (CIF, CIF, CIF)

■ AUTHOR INFORMATION

Corresponding Authors

*E-mail: chenning@suda.edu.cn.
*E-mail: echegoyen@utep.edu.
*E-mail: josepmaria.poblet@urv.cat.

ORCID

Lai Feng: 0000-0003-0278-5502
Mauro Boero: 0000-0002-5052-2849
Antonio Rodríguez-Fortea: 0000-0001-5884-5629
Josep M. Poblet: 0000-0002-4533-0623
Luis Echegoyen: 0000-0003-1107-9423
Ning Chen: 0000-0002-9405-6229

Author Contributions

⊥W.C., L.A., and J.Z. contributed equally to this work.

Notes

The authors declare no competing financial interest.

■ ACKNOWLEDGMENTS

We acknowledge Prof. Shuao Wang (Soochow University) and Prof. Marilyn M. Olmstead (University of California, Davis) for kind technique support and insightful discussions. C.N. thanks the National Science Foundation China (NSFC 51302178) the NSF of Jiangsu Province (BK20171211), Priority Academic Program Development of Jiangsu Higher Education Institutions (PAPD), and the project of scientific and technologic infrastructure of Suzhou (SZS201708). L.E. thanks the US National Science Foundation (NSF) for generous support of this work under the NSF-PREM program (DMR 1205302) and CHE-1801317. The Robert A. Welch Foundation is also gratefully acknowledged for an endowed chair to L.E. (grant AH-0033). J.M.P. and A.R.-F thank the Spanish Ministry of Science (CTQ2017-87269-P) and the Generalitat de Catalunya (2017SGR629 and XRQTC) for support. J.M.P. also thanks ICREA foundation for an ICREA ACADEMIA award. R.M.-M. thanks Spanish Ministry of Science for a PhD fellowship. M.B. thanks HPC - Equipex Equip@Meso/CPER Alsacalcul at the University of Strasbourg, and Grand Equipement National de Calcul Intensif (GENCI) under allocation DARI-A2 A0040906092. Research reported in this article was also partially supported by the National Institute of General Medical Sciences of the National Institutes of Health under linked Award Numbers RL5GM118969, TL4GM118971, and UL1GM118970.

■ REFERENCES

(1) Suzuki, M.; Mizorogi, N.; Yang, T.; Uhlik, F.; Slanina, Z.; Zhao, X.; Yamada, M.; Maeda, Y.; Hasegawa, T.; Nagase, S.; et al. La_2@C_s(17490)-C_{76}: A New Non-IPR Dimetallic Metallofullerene Featuring Unexpectedly Weak Metal−Pentalene Interactions. *Chem. - Eur. J.* **2013**, *19*, 17125−17130.

(2) Chen, C.-H.; Abella, L.; Cerón, M. R.; Guerrero-Ayala, M. A.; Rodríguez-Fortea, A.; Olmstead, M. M.; Powers, X. B.; Balch, A. L.; Poblet, J. M.; Echegoyen, L. Zigzag Sc_2C_2 Carbide Cluster inside a [88]Fullerene Cage with One Heptagon, Sc_2C_2@C_s(hept)-C_{88}: A Kinetically Trapped Fullerene Formed by C_2 Insertion? *J. Am. Chem. Soc.* **2016**, *138*, 13030−13037.

(3) Yamada, M.; Kurihara, H.; Suzuki, M.; Guo, J. D.; Waelchli, M.; Olmstead, M. M.; Balch, A. L.; Nagase, S.; Maeda, Y.; Hasegawa, T.; Lu, X.; Akasaka, T. Sc_2@C_{66} Revisited: An Endohedral Fullerene with Scandium Ions Nestled within Two Unsaturated Linear Triquinanes. *J. Am. Chem. Soc.* **2014**, *136*, 7611−7614.

(4) Schmalz, T.; Seitz, W. A.; Klein, D. J.; Hite, G. Elemental carbon cages. *J. Am. Chem. Soc.* **1988**, *110*, 1113−1127.

(5) Kroto, H. W. The stability of the fullerenes C_{24}, C_{28}, C_{32}, C_{36}, C_{50}, C_{60} and C_{70}. *Nature* **1987**, *329*, 529−531.

(6) Xie, S. Y.; Gao, F.; Lu, X.; Huang, R. B.; Wang, C. R.; Zhang, X.; Liu, M. L.; Deng, S. L.; Zheng, L. S. Capturing the labile fullerene[50] as $C_{50}Cl_{10}$. *Science* **2004**, *304*, 699−699.

(7) Tan, Y. Z.; Zhou, T.; Bao, J. A.; Shan, G. J.; Xie, S. Y.; Huang, R. B.; Zheng, L. S. $C_{72}Cl_4$: A Pristine Fullerene with Favorable Pentagon-Adjacent Structure. *J. Am. Chem. Soc.* **2010**, *132*, 17102−17104.

(8) Tan, Y. Z.; Liao, Z. J.; Qian, Z. Z.; Chen, R. T.; Wu, X.; Liang, H.; Han, X.; Zhu, F.; Zhou, S. J.; Zheng, Z. P.; Lu, X.; Xie, S. Y.; Huang, R. B.; Zheng, L. S. Two I-h-symmetry-breaking C_{60} isomers stabilized by chlorination. *Nat. Mater.* **2008**, *7*, 790−794.

(9) Troshin, P. A.; Avent, A. G.; Darwish, A. D.; Martsinovich, N.; Abdulsada, A. K.; Street, J. M.; Taylor, R. Isolation of Two Seven-Membered Ring C_{58} Fullerene Derivatives: $C_{58}F_{17}CF_3$ and $C_{58}F_{18}$. *Science* **2005**, *309*, 278−281.

(10) Tan, Y. Z.; Li, J.; Zhu, F.; Han, X.; Jiang, W. S.; Huang, R. B.; Zheng, Z. P.; Qian, Z. Z.; Chen, R. T.; Liao, Z. J.; et al. Chlorofullerenes featuring triple sequentially fused pentagons. *Nat. Chem.* **2010**, *2*, 269−273.

(11) Wang, C. R.; Shi, Z. Q.; Wan, L. J.; Lu, X.; Dunsch, L.; Shu, C. Y.; Tang, Y. L.; Shinohara, H. $C_{64}H_4$: Production, isolation, and structural characterizations of a stable unconventional fulleride. *J. Am. Chem. Soc.* **2006**, *128*, 6605−6610.

(12) Tan, Y. Z.; Han, X.; Wu, X.; Meng, Y. Y.; Zhu, F.; Qian, Z. Z.; Liao, Z. J.; Chen, M. H.; Lu, X.; Xie, S. Y.; Huang, R. B.; Zheng, L. S. An Entrant of Smaller Fullerene: C_{56} Captured by Chlorines and Aligned in Linear Chains. *J. Am. Chem. Soc.* **2008**, *130*, 15240−15241.

DOI: 10.1021/jacs.8b10435
J. Am. Chem. Soc. XXXX, XXX, XXX−XXX

(13) Han, X.; Zhou, S. J.; Tan, Y. Z.; Wu, X.; Gao, F.; Liao, Z. J.; Huang, R. B.; Feng, Y. Q.; Lu, X.; Xie, S. Y. Crystal Structures of Saturn-Like $C_{50}Cl_{10}$ and Pineapple-Shaped $C_{64}Cl_4$: Geometric Implications of Double-and Triple-Pentagon-Fused Chlorofullerenes. *Angew. Chem., Int. Ed.* **2008**, *47*, 5340−5343.
(14) Chen, D.-L.; Tian, W. Q.; Feng, J.-K.; Sun, C.-C. Structures and Electronic Properties of $C_{56}Cl_8$ and $C_{56}Cl_{10}$ Fullerene Compounds. *ChemPhysChem* **2007**, *8*, 2386−2390.
(15) Chen, N.; Mulet-Gas, M.; Li, Y. Y.; Stene, R. E.; Atherton, C. W.; Rodriguez-Fortea, A.; Poblet, J. M.; Echegoyen, L. $Sc_2S@C_2(7892)$-C_{70}: a metallic sulfide cluster inside a non-IPR C_{70} cage. *Chem. Sci.* **2013**, *4*, 180−186.
(16) Mercado, B. Q.; Chen, N.; Rodriguez-Fortea, A.; Mackey, M. A.; Stevenson, S.; Echegoyen, L.; Poblet, J. M.; Olmstead, M. H.; Balch, A. L. The Shape of the $Sc_2(\mu 2\text{-}S)$ Unit Trapped in C_{82}: Crystallographic, Computational, and Electrochemical Studies of the Isomers, $Sc_2(\mu 2\text{-}S)@C_s(6)$-$C_{82}$ and $Sc_2(\mu 2\text{-}S)@C_{3v}(8)$-$C_{82}$. *J. Am. Chem. Soc.* **2011**, *133*, 6752−6760.
(17) Stevenson, S.; Fowler, P. W.; Heine, T.; Duchamp, J. C.; Rice, G.; Glass, T.; Harich, K.; Hajdu, E.; Bible, R.; Dorn, H. C. Materials science - A stable non-classical metallofullerene family. *Nature* **2000**, *408*, 427−428.
(18) Shi, Z. Q.; Wu, X.; Wang, C. R.; Lu, X.; Shinohara, H. Isolation and characterization of $Sc_2C_2@C_{68}$: A metal-carbide endofullerene with a non-IPR carbon cage. *Angew. Chem., Int. Ed.* **2006**, *45*, 2107−2111.
(19) Yang, S. F.; Popov, A. A.; Dunsch, L. Violating the Isolated Pentagon Rule (IPR): The endohedral Non-IPR cage of $Sc_3N@C_{70}$. *Angew. Chem., Int. Ed.* **2007**, *46*, 1256−1259.
(20) Zhang, M.; Hao, Y.; Li, X.; Feng, L.; Yang, T.; Wan, Y.; Chen, N.; Slanina, Z. k.; Uhlík, F.; Cong, H. Facile Synthesis of an Extensive Family of $Sc_2O@C_{2n}$ (n = 35−47) and Chemical Insight into the Smallest Member of $Sc_2O@$ $C_2(7892)$−C_{70}. *J. Phys. Chem. C* **2014**, *118*, 28883−28889.
(21) Chen, N.; Beavers, C. M.; Mulet-Gas, M.; Rodríguez-Fortea, A.; Munoz, E. J.; Li, Y.-Y.; Olmstead, M. M.; Balch, A. L.; Poblet, J. M.; Echegoyen, L. $Sc_2S@C_s(10528)$-C_{72}: A dimetallic sulfide endohedral fullerene with a non Isolated Pentagon Rule cage. *J. Am. Chem. Soc.* **2012**, *134*, 7851−7860.
(22) Yamada, M.; Wakahara, T.; Tsuchiya, T.; Maeda, Y.; Akasaka, T.; Mizorogi, N.; Nagase, S. Spectroscopic and Theoretical Study of Endohedral Dimetallofullerene Having a Non-IPR Fullerene Cage: $Ce_2@C_{72}$. *J. Phys. Chem. A* **2008**, *112*, 7627−7631.
(23) Kato, H.; Taninaka, A.; Sugai, T.; Shinohara, H. Structure of a Missing-Caged Metallofullerene: $La_2@C_{72}$. *J. Am. Chem. Soc.* **2003**, *125*, 7782−7783.
(24) Yang, S.; Popov, A. A.; Dunsch, L. The Role of an Asymmetric Nitride Cluster on a Fullerene Cage: The Non-IPR Endohedral $DySc_2N@C_{76}$. *J. Phys. Chem. B* **2007**, *111*, 13659−13663.
(25) Popov, A. A.; Krause, M.; Yang, S. F.; Wong, J.; Dunsch, L. C_{78} cage isomerism defined by trimetallic nitride cluster size: A computational and vibrational spectroscopic study. *J. Phys. Chem. B* **2007**, *111*, 3363−3369.
(26) Yang, S. F.; Dunsch, L. A large family of dysprosium-based trimetallic nitride endohedral fullerenes: $Dy_3N@C_{2n}$ ($39 \le n \le 44$). *J. Phys. Chem. B* **2005**, *109*, 12320−12328.
(27) Fu, W.; Xu, L.; Azurmendi, H.; Ge, J.; Fuhrer, T.; Zuo, T.; Reid, J.; Shu, C.; Harich, K.; Dorn, H. C. ^{89}Y and ^{13}C NMR Cluster and Carbon Cage Studies of an Yttrium Metallofullerene Family, $Y_3N@C_{2n}$ (n = 40− 43). *J. Am. Chem. Soc.* **2009**, *131*, 11762−11769.
(28) Alegret, N.; Chaur, M. N.; Santos, E.; Rodríguez-Fortea, A.; Echegoyen, L.; Poblet, J. M. Bingel−Hirsch Reactions on Non-IPR $Gd_3N@C_{2n}$ ($2n$ = 82 and 84). *J. Org. Chem.* **2010**, *75*, 8299−8302.
(29) Beavers, C. M.; Zuo, T. M.; Duchamp, J. C.; Harich, K.; Dorn, H. C.; Olmstead, M. M.; Balch, A. L. $Tb_3N@C_{84}$: An improbable, egg-shaped endohedral fullerene that violates the isolated pentagon rule. *J. Am. Chem. Soc.* **2006**, *128*, 11352−11353.
(30) Slanina, Z.; Kobayashi, K.; Nagase, S. $Ca@C_{72}$ IPR and non-IPR structures: computed temperature development of their relative concentrations. *Chem. Phys. Lett.* **2003**, *372*, 810−814.
(31) Yang, T.; Zhao, X.; Xu, Q.; Zhou, C.; He, L.; Nagase, S. Non-IPR endohedral fullerene $Yb@C_{76}$: density functional theory characterization. *J. Mater. Chem.* **2011**, *21*, 12206−12209.
(32) Yang, T.; Zhao, X.; Xu, Q.; Zheng, H.; Wang, W.-W.; Li, S.-T. Probing the role of encapsulated alkaline earth metal atoms in endohedral metallofullerenes $M@C_{76}$ (M = Ca, Sr, and Ba) by first-principles calculations. *Dalton Trans* **2012**, *41*, 5294−5300.
(33) Hao, Y. J.; Feng, L.; Xu, W.; Gu, Z. G.; Hu, Z. Q.; Shi, Z. J.; Slanina, Z.; Uhlik, F. $Sm@C_{2v}(19138)$-C_{76}: A Non-IPR Cage Stabilized by a Divalent Metal Ion. *Inorg. Chem.* **2015**, *54*, 4243−4248.
(34) Zhao, P.; Zhao, X.; Ehara, M. Theoretical Insights into Monometallofullerene $Th@C_{76}$: Strong Covalent Interaction between Thorium and the Carbon Cage. *Inorg. Chem.* **2018**, *57*, 2961−2964.
(35) Wakahara, T.; Nikawa, H.; Kikuchi, T.; Nakahodo, T.; Rahman, G. M. A.; Tsuchiya, T.; Maeda, Y.; Akasaka, T.; Yoza, K.; Horn, E.; Yamamoto, K.; Mizorogi, N.; Slanina, Z.; Nagase, S. $La@C_{72}$ having a non-IPR carbon cage. *J. Am. Chem. Soc.* **2006**, *128*, 14228−14229.
(36) Cai, W.; Morales-Martínez, R.; Zhang, X.; Najera, D.; Romero, E. L.; Metta-Magaña, A.; Rodríguez-Fortea, A.; Fortier, S.; Chen, N.; Poblet, J. M.; Echegoyen, L. Single crystal structures and theoretical calculations of uranium endohedral metallofullerenes ($U@C_{2n}$, $2n$ = 74, 82) show cage isomer dependent oxidation states for U. *Chem. Sci.* **2017**, *8*, 5282−5290.
(37) Li, Y.; Yang, L.; Liu, C.; Hou, Q.; Jin, P.; Lu, X. Th-Based Endohedral Metallofullerenes: Anomalous Metal Position and Significant Metal-Cage Covalent Interactions with the Involvement of Th 5f Orbitals. *Inorg. Chem.* **2018**, *57*, 7142−7150.
(38) Wang, Y.; Morales-Martínez, R.; Zhang, X.; Yang, W.; Wang, Y.; Rodríguez-Fortea, A.; Poblet, J. M.; Feng, L.; Wang, S.; Chen, N. Unique Four-Electron Metal-to-Cage Charge Transfer of Th to a C_{82} Fullerene Cage: Complete Structural Characterization of $Th@C_{3v}(8)$-C_{82}. *J. Am. Chem. Soc.* **2017**, *139*, 5110−5116.
(39) Zhang, X.; Li, W.; Feng, L.; Chen, X.; Hansen, A.; Grimme, S.; Fortier, S.; Sergentu, D.-C.; Duignan, T. J.; Autschbach, J.; et al. A diuranium carbide cluster stabilized inside a C_{80} fullerene cage. *Nat. Commun.* **2018**, *9*, 2753.
(40) Zhang, X.; Wang, Y.; Morales-Martínez, R.; Zhong, J.; de Graaf, C.; Rodríguez-Fortea, A.; Poblet, J. M.; Echegoyen, L.; Feng, L.; Chen, N. $U_2@I_h(7)$-C_{80}: Crystallographic Characterization of a Long-Sought Dimetallic Actinide Endohedral Fullerene. *J. Am. Chem. Soc.* **2018**, *140*, 3907−3915.
(41) Akiyama, K.; Zhao, Y.; Sueki, K.; Tsukada, K.; Haba, H.; Nagame, Y.; Kodama, T.; Suzuki, S.; Ohtsuki, T.; Sakaguchi, M.; Kikuchi, K.; Katada, M.; Nakahara, H. Isolation and Characterization of Light Actinide Metallofullerenes. *J. Am. Chem. Soc.* **2001**, *123*, 181−182.
(42) Liddle, S. T. The Renaissance of Non-Aqueous Uranium Chemistry. *Angew. Chem., Int. Ed.* **2015**, *54*, 8604−8641.
(43) Hayton, T. W. Recent developments in actinide-ligand multiple bonding. *Chem. Commun.* **2013**, *49*, 2956−2973.
(44) Krätschmer, W.; Lamb, L. D.; Fostiropoulos, K.; Huffman, D. R. Solid C60: a new form of carbon. *Nature* **1990**, *347*, 354−358.
(45) Olmstead, M. H.; de Bettencourt-Dias, A.; Duchamp, J. C.; Stevenson, S.; Marciu, D.; Dorn, H. C.; Balch, A. L. Isolation and structural characterization of the endohedral fullerene $Sc_3N@C_{78}$. *Angew. Chem., Int. Ed.* **2001**, *40*, 1223−1225.
(46) Zuo, T. M.; Beavers, C. M.; Duchamp, J. C.; Campbell, A.; Dorn, H. C.; Olmstead, M. M.; Balch, A. L. Isolation and structural characterization of a family of endohedral fullerenes including the large, chiral cage fullerenes $Tb_3N@C_{88}$ and $Tb_3N@C_{86}$ as well as the I_h and D_{5h} isomers of $Tb_3N@C_{80}$. *J. Am. Chem. Soc.* **2007**, *129*, 2035−2043.
(47) Rodríguez-Fortea, A.; Alegret, N.; Balch, A. L.; Poblet, J. M. The maximum pentagon separation rule provides a guideline for the structures of endohedral metallofullerenes. *Nat. Chem.* **2010**, *2*, 955.
(48) Slanina, Z.; Lee, S.-L.; Uhlík, F.; Adamowicz, L.; Nagase, S. Computing relative stabilities of metallofullerenes by Gibbs energy treatments. *Theor. Chem. Acc.* **2007**, *117*, 315−322.

DOI: 10.1021/jacs.8b10435
J. Am. Chem. Soc. XXXX, XXX, XXX−XXX

(49) Slanina, Z.; Nagase, S. $Sc_3N@C_{80}$: Computations on the Two-Isomer Equilibrium at High Temperatures. *ChemPhysChem* **2005**, *6*, 2060−2063.
(50) Slanina, Z.; Adamowicz, L. On the relative stabilities of dodecahedron-shaped and bowl-shaped structures of C_{20}. *Thermochim. Acta* **1992**, *205*, 299−306.
(51) Fowler, P.; Manolopoulos, D. *An Atlas of Fullerenes*; Oxford University Press: Oxford, U.K., 1995.
(52) Tang, Q.; Abella, L.; Hao, Y.; Li, X.; Wan, Y.; Rodríguez-Fortea, A.; Poblet, J. M.; Feng, L.; Chen, N. $Sc_2O@C_{2v}(5)$-C_{80}: Dimetallic Oxide Cluster Inside a C_{80} Fullerene Cage. *Inorg. Chem.* **2015**, *54*, 9845−9852.
(53) Stevenson, S.; Rice, G.; Glass, T.; Harich, K.; Cromer, F.; Jordan, M. R.; Craft, J.; Hadju, E.; Bible, R.; Olmstead, M. M.; Maitra, K.; Fisher, A. J.; Balch, A. L.; Dorn, H. C. Small-bandgap endohedral metallofullerenes in high yield and purity. *Nature* **1999**, *401*, 55.
(54) Popov, A. A.; Dunsch, L. Structure, Stability, and Cluster-Cage Interactions in Nitride Clusterfullerenes $M_3N@C_{2n}$ (M = Sc, Y; $2n$ = 68−98): a Density Functional Theory Study. *J. Am. Chem. Soc.* **2007**, *129*, 11835−11849.
(55) Chaur, M. N.; Valencia, R.; Rodríguez-Fortea, A.; Poblet, J. M.; Echegoyen, L. Trimetallic Nitride Endohedral Fullerenes: Experimental and Theoretical Evidence for the $M_3N^{6+}@C_{2n}^{6-}$ model. *Angew. Chem., Int. Ed.* **2009**, *48*, 1425−1428.
(56) Campanera, J. M.; Bo, C.; Poblet, J. M. General Rule for the Stabilization of Fullerene Cages Encapsulating Trimetallic Nitride Templates. *Angew. Chem., Int. Ed.* **2005**, *44*, 7230−7233.
(57) Popov, A. A.; Yang, S.; Dunsch, L. Endohedral Fullerenes. *Chem. Rev.* **2013**, *113*, 5989−6113.
(58) Nishibori, E.; Takata, M.; Sakata, M.; Taninaka, A.; Shinohara, H. Pentagonal-Dodecahedral La2 Charge Density in [80-I_h]Fullerene: $La_2@C_{80}$. *Angew. Chem., Int. Ed.* **2001**, *40*, 2998−2999.
(59) Akasaka, T.; Nagase, S.; Kobayashi, K.; Wälchli, M.; Yamamoto, K.; Funasaka, H.; Kako, M.; Hoshino, T.; Erata, T. ^{13}C and ^{139}La NMR Studies of $La_2@C_{80}$: First Evidence for Circular Motion of Metal Atoms in Endohedral Dimetallofullerenes. *Angew. Chem., Int. Ed. Engl.* **1997**, *36*, 1643−1645.
(60) Popov, A. A.; Avdoshenko, S. M.; Pendás, A. M.; Dunsch, L. Bonding between strongly repulsive metal atoms: an oxymoron made real in a confined space of endohedral metallofullerenes. *Chem. Commun.* **2012**, *48*, 8031−8050.
(61) Popov, A. A.; Dunsch, L. Bonding in Endohedral Metallofullerenes as Studied by Quantum Theory of Atoms in Molecules. *Chem. - Eur. J.* **2009**, *15*, 9707−9729.
(62) Bader, R. F. W. *Atoms in Molecules: A Quantum Theory*; Oxford University Press: Oxford, U.K., 1990.
(63) Sheldrick, G. M. *Acta Crystallogr., Sect. A: Found. Crystallogr.* **2008**, *64*, 112−122.
(64) Baerends, E. J. E., D. E; Ros, P. *ADF*, 2013.01; SCM: Amsterdam, 2013.
(65) te Velde, G.; Bickelhaupt, F. M.; Baerends, E. J.; Fonseca Guerra, C.; van Gisbergen, S. J. A.; Snijders, J. G.; Ziegler, T. Chemistry with ADF. *J. Comput. Chem.* **2001**, *22*, 931−967.
(66) *CPMD* 4.1; IBM Corp.: Armonk, NY, 2015.
(67) Car, R.; Parrinello, M. Unified Approach for Molecular Dynamics and Density-Functional Theory. *Phys. Rev. Lett.* **1985**, *55*, 2471−2474.
(68) Lu, T.; Chen, F. Multiwfn: A multifunctional wavefunction analyzer. *J. Comput. Chem.* **2012**, *33*, 580−592.
(69) Frisch, M. J.; Trucks, G. W.; Schlegel, H. B.; Scuseria, G. E.; Robb, M. A.; Cheeseman, J. R.; Scalmani, G.; Barone, V.; Petersson, G. A.; Nakatsuji, H.; Li, X.; Caricato, M.; Marenich, A. V.; Bloino, J.; Janesko, B. G.; Gomperts, R.; Mennucci, B.; Hratchian, H. P.; Ortiz, J. V.; Izmaylov, A. F.; Sonnenberg, J. L.; Williams-Young, D.; Ding, F.; Lipparini, F.; Egidi, F.; Goings, J.; Peng, B.; Petrone, A.; Henderson, T.; Ranasinghe, D.; Zakrzewski, V. G.; Gao, J.; Rega, N.; Zheng, G.; Liang, W.; Hada, M.; Ehara, M.; Toyota, K.; Fukuda, R.; Hasegawa, J.; Ishida, M.; Nakajima, T.; Honda, Y.; Kitao, O.; Nakai, H.; Vreven, T.; Throssell, K.; Montgomery, J. A., Jr.; Peralta, J. E.; Ogliaro, F.; Bearpark, M.; Heyd, J. J.; Brothers, E. N.; Kudin, K. N.; Staroverov, V. N.; Kobayashi, R.; Normand, J.; Raghavachari, K.; Rendell, A.; Burant, J. C.; Iyengar, S. S.; Tomasi, J.; Cossi, M.; Millam, J. M.; Klene, M.; Adamo, C.; Cammi, R.; Ochterski, J. W.; Martin, R. L.; Morokuma, K.; Farkas, O.; Foresman, J. B.; Fox, D. J. *Gaussian 16*, revision A.03; Gaussian, Inc.: Wallingford CT, 2016.
(70) Cao, X.; Dolg, M. Segmented contraction scheme for small-core lanthanide pseudopotential basis sets. *J. Mol. Struct.: THEOCHEM* **2002**, *581*, 139−147.
(71) Álvarez-Moreno, M.; de Graaf, C.; López, N.; Maseras, F.; Poblet, J. M.; Bo, C. Managing the Computational Chemistry Big Data Problem: The ioChem-BD Platform. *J. Chem. Inf. Model.* **2015**, *55*, 95−103.

DOI: 10.1021/jacs.8b10435
J. Am. Chem. Soc. XXXX, XXX, XXX−XXX